SEPTEMBER 27 2021

Incorporating direct metal laser sintered complex shaped Ti-6Al-4V components in ultrasonic surgical devices[a)]

Special Collection: Additive Manufacturing and Acoustics

Rebecca Cleary ; Xuan Li ; Margaret Lucas

J. Acoust. Soc. Am. 150, 2163–2173 (2021)
https://doi.org/10.1121/10.0006379

JASA ARTICLE

Incorporating direct metal laser sintered complex shaped Ti-6Al-4V components in ultrasonic surgical devices[a]

Rebecca Cleary,[b] Xuan Li,[c] and Margaret Lucas[d]
Centre for Medical & Industrial Ultrasonics, James Watt School of Engineering, University of Glasgow, Glasgow, G12 8QQ, Scotland, United Kingdom

ABSTRACT:
Additive manufacturing (AM) offers opportunities to design more complex shapes of the Ti-6Al-4V parts commonly used in high-power ultrasonic surgical devices. Moreover, AM metal printing will be essential to the realization of miniature ultrasonic devices incorporating internal structures for minimally invasive surgical procedures. However, it is necessary first to verify the ultrasonic vibrational behavior of devices with three-dimensional (3D) printed metal parts. Therefore, two different prototype devices are fabricated, with CNC machined mill annealed and 3D printed Ti-6Al-4V parts. Both devices, an ultrasonic bone needle and a miniature ultrasonic scalpel, incorporate complex geometries but can be manufactured using subtractive processes so that the comparative effects of 3D printing on the vibrational performance of the devices can be elucidated. The metal microstructure is investigated through measurements of longitudinal and shear acoustic velocities and scanning electron microscopy. Comparisons of electrical impedance, frequency and modal responses, and the vibrational response at increasing levels of excitation enable evaluation of the efficacy of incorporating 3D printed Ti-6Al-4V parts. Results show that whereas the bone needle exhibited comparable vibrational responses for the measurement techniques used, the 3D printed bone cutting device exhibited a more dense modal response and developed cracks at high excitation levels.

https://doi.org/10.1121/10.0006379

(Received 22 February 2021; revised 24 August 2021; accepted 26 August 2021; published online 27 September 2021)
[Editor: Michael R Haberman] Pages: 2163–2173

I. INTRODUCTION

High-power ultrasonic devices have been adopted for a range of surgical procedures, offering precision, tissue selectivity, improved hemostasis, and reduced injury to surrounding tissue. Applications include tissue resection and bone osteotomy in maxillofacial,[1] orthodontic,[2] cranial,[3] and spinal[4,5] surgeries. However, there remain many surgical procedures that could benefit from ultrasonic surgical devices, but viable device designs have not yet been realized, especially for minimally invasive surgeries. Challenges lie in generating sufficient vibrational amplitude at the surgical tip within the geometric constraints imposed by both the device and surgical procedure.

An example of a surgical application that could benefit from a new approach to device design is deep bone cutting in orthopedics, where current popular devices, such as sagittal saws, drills, and burrs, often result in damage to surrounding tissues[6] and a large zone of thermal necrosis around the cut site, which is known to delay healing.[7] Ultrasonic devices offer a promising alternative, requiring low cutting force and low micro-damage at the cut site.[8] However, delivering ultrasonic vibration to a surgical tip, where the amplitude and mode of vibration can allow deep penetration into bone, is hampered by a number of key design issues. Ultrasonic surgical devices are driven in resonance by a Langevin-style transducer at a low ultrasonic frequency (usually in the 20–40 kHz range) to achieve a sufficient vibrational amplitude, and this limits the geometry to one half-wavelength or a multiple of a half-wavelength of the first longitudinal mode (L1) at the driving frequency. Bone cutting requires a slender, typically less than 5 mm,[9] and sharp cutting tip, and deep penetration requires a longer slender tip. These attributes tend to increase the modal density around the L1 modal frequency, making it more difficult to avoid exciting parasitic modes.[10] Further, it has been shown that devices with long slender cutting tips exhibit strong nonlinear responses at the excitation levels typical of high power ultrasonic surgical devices. These result in resonance frequency shifts, amplitude saturation, jump phenomenon, and unstable operating regimes,[11] making the device unusable. This has been a key reason why commercial devices are limited to shallow cuts.

An opportunity for minimally invasive surgeries is to employ smaller ultrasonic surgical devices which could be integrated with surgical robots, enabling more procedures to be carried out in out-patient clinics or as day surgeries. For a Langevin-style ultrasonic surgical device an immediate

---

[a] This paper is part of a special issue on ADDITIVE MANUFACTURING AND ACOUSTICS.
[b] ORCID: 0000-0001-5497-6170.
[c] ORCID: 0000-0002-5655-8631.
[d] Electronic mail: margaret.lucas@glasgow.ac.uk ORCID: 0000-0002-3625-9714.

solution to reduce its size from the current typically 25 kHz one wavelength configuration, is to contain the whole device (transducer plus surgical tip) into one half-wavelength of the L1 mode frequency and tune its resonance at a higher frequency. The challenge here is to deliver sufficient vibrational displacement amplitude to cut bone despite the lower volume of piezoceramic material in the transducer and the higher ratio of slender tip length to device length.

There are potential design solutions for small devices, which could deliver much higher vibrational displacement amplification, from the piezoelectric material to the surgical tip, than a conventional Langevin transducer design. These designs would incorporate geometrical features in the front mass of the transducer that are known to increase vibrational displacement, including slots, helical cuts, and voids. Where these features are internal to the front mass, they cannot be realized through subtractive manufacturing techniques.

Additive manufacturing (AM) offers a promising technique for creating customizable and complex structures and this has been demonstrated in customizable actuators and sensors which have been fabricated in a single step with sufficient resolution to create micro-scale features with high precision.[12,13] Also, some ultrasonic devices such as piezoceramic actuators and arrays have been shown to deliver enhanced performance using additive manufacturing.[14–16] Recently, a simple configuration of a high power Langevin ultrasonic transducer, where three-dimensional (3D) metal printing was used to fabricate the Ti-6Al-4V cylindrical end masses, was shown to exhibit vibrational performance characteristics that closely match those where the end masses were CNC machined from a mill annealed Ti-6Al-4V bar.[17]

However, the use of AM has not been demonstrated in ultrasonic surgical devices or in any Langevin-style ultrasonic device featuring complex geometries. Therefore, before adopting AM to realize designs that cannot be manufactured using subtractive techniques, we aim to evaluate AM in two prototype devices whose front masses can be 3D printed or machined. Both devices incorporate geometrical features in the front mass that result in very different vibrational motions. We also aim to demonstrate the effectiveness of vibration characterization techniques in distinguishing the vibrational behavior of devices with metal masses of the same alloy, Ti-6Al-4V, but different microstructures.

To illustrate this, we compare devices incorporating metal parts created by additive manufacturing with those created by subtractive manufacturing. For this purpose, we have designed two different devices, an ultrasonic needle for deep bone penetration and a small surgical bone cutting device. The choice of devices is governed by the fact that they are challenging but possible to fabricate using subtractive manufacturing techniques and they are currently the basic design configurations for future developments that will incorporate geometries and features only achievable through additive manufacturing. For both devices, the metal masses (the transducer back mass and surgical tip) are Ti-6Al-4V, with the AM parts fabricated using direct metal laser sintering (DMLS) (EOS M280, Protolabs, UK) and the others CNC machined from a mill annealed (MA) bar.

II. MATERIAL PROPERTIES OF Ti-6AL-4V

A. Methodology

The properties and microstructure of the materials are first considered. Ultrasonic devices are modelled and tuned using finite element analysis (FEA) (Abaqus, Dassault Systèmes), which relies on input of accurate material properties and therefore these are extracted from measurements of the wave velocities. These measurements are also useful to understand how the material properties that affect vibrational behavior, especially density and stiffness properties, compare between mill annealed and printed Ti-6Al-4V.

Time-of-flight tests were carried out on cube samples ($1\,\mathrm{cm}^3$) of the metals, with surfaces machined to ensure the necessary parallel and low roughness faces. The build resolutions for printed Ti-6Al-4V able to create the features of the front masses of the ultrasonic devices were $30\,\mu$m and $60\,\mu$m and these resolutions were therefore also used for the printed cube samples. A 10 MHz longitudinal wave transducer (Olympus V312-SU) and a 20 MHz shear wave transducer (Olympus V222-BA-RM), both connected to a pulse-receiver (JSR DPR300) and an oscilloscope (Keysight DSOX3014A), were used to measure the longitudinal, V_L, and shear wave, V_S, velocities, respectively, with each measurement repeated three times. The acoustic velocities and sample density, ρ, calculated by measuring the sample mass and volume, were then used to calculate the Poisson's ratio, ν, Young's modulus, E, and shear modulus, G, from Eqs. (1), (2), and (3),

$$\nu = \frac{1 - 2(V_S/V_L)^2}{2 - 2(V_S/V_L)^2}, \tag{1}$$

$$E = \frac{{V_L}^2 \rho (1+\nu)(1-2\nu)}{1-\nu}, \tag{2}$$

$$G = {V_S}^2 \rho. \tag{3}$$

It is known that even small variations in the microstructure of Ti-6Al-4V affect the vibrational behavior, including the tuning, of ultrasonic surgical devices. Manufacturers and materials suppliers tightly control consistency in the batch to batch microstructure of the MA bar from which device components are machined.[18] It is therefore important to evaluate AM in terms of the difference in micro-structure between DMLS components and those machined from MA bar, how micro-structure is affected by the resolution of DMLS, and also the consistency of a DMLS component's microstructure. Scanning electron microscopy (SEM) was therefore used to image samples created from the metal cubes, combining backscattered electron imaging (BSE), to identify the grain structure and phase composition, and electron backscatter diffraction imaging (EBSD), to identify the crystallographic orientation. These results are then also used

TABLE I. Material properties from time-of-flight tests.

Sample type Ti-6Al-4V	Longitudinal wave velocity (m/s)	Shear wave velocity (m/s)	Density (kg/m^3)	Young's Modulus (GPa)	Shear Modulus (GPa)	Poisson's Ratio
MA supplier properties			4430	114.0		0.330
MA	6171 ± 0.1%	3157 ± 0.7%	4397 ± 0.4%	115.9	32.2	0.323
30μm DMLS	6242 ± 0%	3189 ± 0.4%	4259 ± 0.5%	114.6	32.9	0.323
60μm DMLS	6273 ± 0.2%	3136 ± 0.6%	4250 ± 0.2%	111.5	32.8	0.333

to determine the effects of the microstructure on the vibrational behavior of the ultrasonic devices.

B. Results

The material properties calculated from the time-of-flight measurements are presented in Table I. It is notable that the shear wave velocities of all samples are consistent and all within the typical range of MA bar for Ti-6Al-4V. However, the longitudinal velocities of the DMLS samples are around 1%–2% higher and densities around 3% lower than samples from MA bar, contributing to a marginally lower Young's modulus of 111.5 GPa for the 60 μm resolution DMLS samples. The Poisson's ratio varies minimally due to its dependency on the ratio of the wave velocities which does not change significantly. As an example of the effects of these results on frequency tuning, a simple titanium bar was modelled in FEA with the L1 mode tuned to 20 kHz using the measured properties of MA Ti-6Al-4V. For the same bar dimensions, the L1 frequency for the 60 μm resolution DMLS was 50 Hz lower and for 30 μm resolution DMLS was 200 Hz higher. This shows that resonance frequency is less than 1% different between the materials, which is within the typical material specification range for tuning surgical devices.

The micrographs in Fig. 1 show the microstructure of samples cut from mill annealed (MA), and 30 and 60 μm DMLS Ti-6Al-4V, scanned along the axial plane or build direction. The MA samples have mainly globular grains without a dominant orientation, consistent with the expected equilibrium microstructure at room temperature. Both DMLS samples have smaller needle or irregular columnar shaped grains caused by the epitaxial growth of the grains in previous layers due to the high-temperature gradient and solidification rate in the molten pool.[19] Their microstructure has pockets of local grain orientations (exhibited as areas of dominant color in the micrographs).

Local grain orientations, or microtextures, are known to result in reduced local stress concentrations,[20] which could be a benefit in high power ultrasonic devices that operate in resonance with large oscillatory displacement amplitude (cyclic strain).[21] However, large areas of microtextures in titanium alloys have been directly related to increased acoustic attenuation,[22] an indicator of lower achievable vibration amplitude in ultrasonic devices. Increased attenuation has also been related to columnar shaped grains as compared with equiaxed grains.[23]

Grain size, in terms of grain area distribution, obtained using orientation imaging microscopy analysis software, is shown in Fig. 2. It has been proposed that uniformity of grain size benefits high power ultrasonic devices, resulting in improved acoustic efficiency and reduced nonlinearity in the vibration response, as well as contributing to higher strength Ti-6Al-4V.[24] The MA sample has a much narrower range of grain sizes but much larger grains, whereas the DMLS samples have smaller grains but with more widely distributed sizes. However, it is unknown how microstructures consisting of columnar shaped grains affect the vibrational response of ultrasonic devices that operate in resonance or whether grain size and size distribution are important parameters in evaluating these effects.

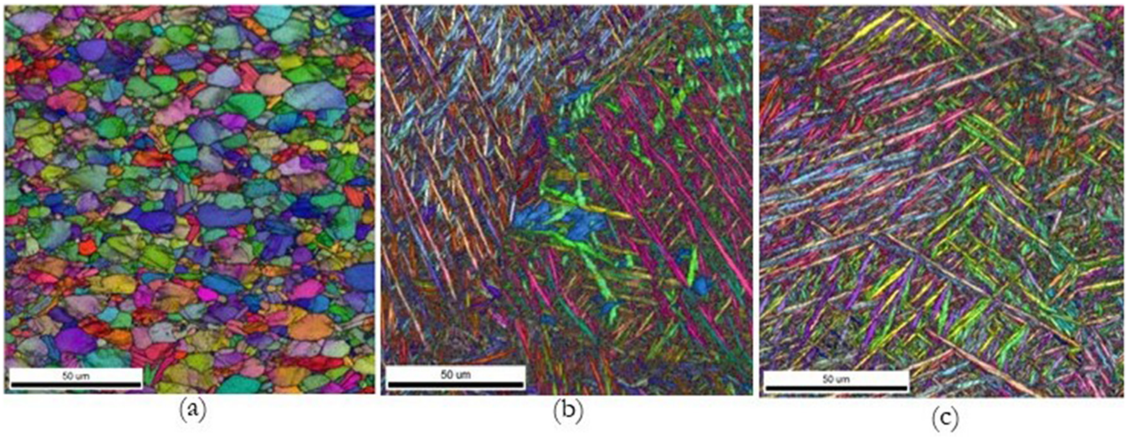

FIG. 1. (Color online) Microstructures of Ti-6Al-4V samples (cut from the 1 cm^3 cubes) and scanned in the build direction (a) MA; and DMLS at (b) 60 μm and (c) 30 μm resolutions.

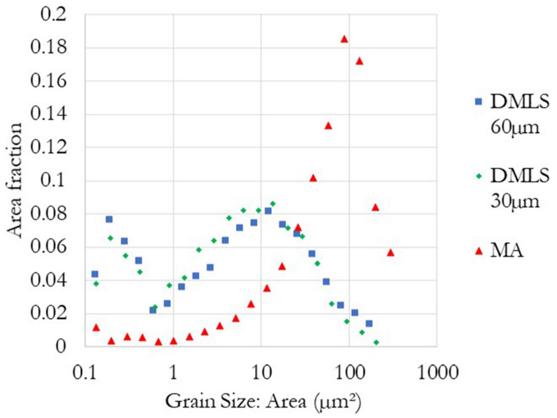

FIG. 2. (Color online) Grain size (area fraction) distribution of Ti-6Al-4V samples (cut from the 1 cm^3 cubes).

To explore the links between the sample material microstructure and the resulting device vibrational behavior, two ultrasonic surgical devices are designed with very different geometries and vibration modes. By creating two geometrically identical versions of each device, one from MA and the other from DMLS Ti-6Al-4V, direct comparisons of vibrational behaviors can provide evidence of the pros and cons of adopting DMLS for manufacture of power ultrasonic devices.

III. ULTRASONIC BONE CUTTING DEVICES

For the two ultrasonic devices, no post-process surface finishing was carried out on the DMLS Ti-6Al-4V parts, apart from polishing of the surfaces that mate with the piezoceramic discs. This was for two reasons; so that the measured vibrational responses could be related to microstructure and build without additional effects of other subtractive surface finishing processes, and so the effects of build quality could be evaluated in terms of future needs. The opportunity lies in designing internal features in 3D printed devices where secondary subtractive processing might not be possible.

A. Ultrasonic bone penetrating needle

The bone penetrating needle has been researched as part of a study to find a solution for surgical access to the petrous apex. The petrous apex is located in the temporal bone and is one of the most difficult areas for surgeons to access because it is in the central region of the skull and close to several neural structures. The petrous apex can be a site of lesions, associated with a number of diseases which are almost impossible to biopsy, and therefore current diagnostics rely wholly on CT and MRI imaging.[25]

The ultrasonic needle (Fig. 3) is in the form of a bolted Langevin transducer with two 20 mm diameter, 4 mm thickness PZT-26 (Meggitt, Denmark) piezoceramic rings sandwiched between two Ti-6Al-4V end masses. The front and back masses have lengths of 91 and 12 mm, respectively. The front mass has a conical taper with helical slots incorporated to convert the axial motion of the piezoceramic rings into combined longitudinal-torsional (L-T) vibration of the needle. L-T mode vibration of the needle tip has been shown to deliver a faster and more precise bone cut with less thermal damage at and surrounding the cut site, than purely longitudinal vibration.[26] The needle was designed in FEA with the front mass and needle shape selected as a best combination of achievable L and T displacement amplitudes and frequency spacing of the L-T mode from neighboring parasitic modes, particularly to prevent flexural vibrations of the needle. The device is tuned to the second L-T mode (L-T2) at a nominal 45 kHz to allow for the required needle length and for the piezoceramic stack to be located at a nodal plane. The proposed needle tip is a symmetrical four point cutting tip inspired by a Franseen needle.

FIG. 3. (Color online) Ultrasonic needles with (a) MA and (b) DMLS Ti-6Al-4V components.

The Ti-6Al-4V components of the two ultrasonic needles were manufactured by CNC machining of the MA bar and through DMLS, with the tapered front mass with helical cuts and the needle being a single part in both devices. The 3D printed DMLS parts have an axial build direction and a build layer thickness of 60 μm. A threaded hole was machined in the front mass to accommodate an M5 prestress bolt.

B. Ultrasonic bone cutting device with planar twice folded front mass

Small ultrasonic bone cutting devices are being researched as part of a study to deliver innovations for minimally invasive surgeries, with a potential for integration with surgical robots. The dimensions are therefore constrained by the size requirement for such tools. Here, we consider a surgical cutting device of 10 mm in diameter and 55 mm in length. It is possible to create a device within these dimensions that is tuned to the L1 mode at around 50 kHz by configuring the cutting blade into the front mass so that the whole device is a half-wavelength. However, this configuration cannot excite sufficient ultrasonic vibration displacement amplitude to cut through bone as effectively as current commercial devices, which are larger and generally operate at a frequency in the 20–30 kHz range. This is a significant challenge for miniaturizing power ultrasonic devices. It is known that there is a linear relationship between power density and frequency. Also, if a transducer's axial dimension is scaled inversely with longitudinal frequency, then the piezoceramic volume will vary inversely with cube of the frequency. This means the available power varies inversely with the square of the frequency. So, a target has been to design a low frequency device that can excite a higher amplitude of vibration at the surgical tip within the size constraints of 10 mm diameter and 55 mm length.

One design of a small ultrasonic bone cutting device is shown in Fig. 4, based on a bolted Langevin transducer and incorporating four 10 mm diameter, 2 mm thickness piezoceramic rings (PIC-181, PI Ceramic). The back mass and front mass have lengths of 19.5 and 26.5 mm, respectively, with the folded front mass having 0.5 mm gaps between the pillars. The configuration of a folded horn was first described for an ultrasonic-sonic percussive planetary exploration tool[27] and has been adapted here to create a different version that is planar and twice folded. The central pillar tapers to a sharp chisel-shaped cutting tip as a demonstrator prototype, but this shape can be tailored for specific surgical procedures. The whole device is tuned to operate in the L1 mode close to 20 kHz.

The device in Fig. 4(a) was manufactured by CNC turning combined with a spark erosion process from MA Ti-6Al-4V bar. The 3D printed DMLS metal components, Fig. 4(b), were fabricated with an axial build direction and a build layer thickness of 30 μm.

IV. EXPERIMENTAL CHARACTERIZATION OF DEVICES

A. Methodology

The methodology comprises three measurement techniques that we routinely use to characterize power ultrasonic devices; impedance analysis, experimental modal analysis (EMA), and harmonic analysis. Impedance analysis and EMA measure electromechanical and resonance characteristics at low excitation levels and therefore in the linear vibrational response regime of the devices. Such techniques can elucidate the variations between MA and DMLS devices in terms of resonance and antiresonance frequencies, electromechanical coupling, losses, and modal parameters (frequency, mode shape, modal damping). These can then be related to the different material microstructural properties in Figs. 1 and 2, as well as the resolution and macrostructure from the manufacturing processes themselves. Harmonic analysis provides a detailed characterization of the device's vibrational response in a small frequency range through its tuned resonance frequency at incrementally increasing excitation levels. It is capable of showing any changes in the excitation threshold of the linear response, between MA and DMLS devices, and can also reveal distinguishing features of the linear or nonlinear response that could relate to the material microstructure or macrostructure at excitation levels typical of device operating conditions.


(a) (b)

FIG. 4. (Color online) Ultrasonic planar twice folded bone cutting devices with (a) MA and (b) DMLS Ti-6Al-4V components.

1. Impedance analysis

The electrical characteristics of the fabricated devices were derived from impedance analysis (IA) using an impedance analyzer (Agilent 4294 A) excited at 1 V_{pp}, over a bandwidth covering the frequency range of interest. The effective electromechanical coupling coefficient, k_{eff}, was calculated from the impedance spectrum data. ${k_{\mathrm{eff}}}^2$ provides a measure of the device's conversion efficiency from electrical energy to mechanical vibrational energy, Eq. (4),[28]

$$ {k_{\mathrm{eff}}}^2 = 1 - \frac{f_r^2}{f_a^2}, \tag{4} $$

where f_r and f_a are the resonance and anti-resonance frequencies, respectively. The quality factor, Q, can also be calculated from the impedance spectrum, as a measure of loss and therefore an indicator of the potential for the device to be excited at a high amplitude of vibration displacement in resonance, but only in the linear response regime of the device.

2. Experimental modal analysis

EMA was performed to characterize the modal response. The devices were excited with a broadband random excitation signal, over a frequency range of 0 to 80 kHz, using data acquisition hardware with an incorporated function generator (Quattro, Data Physics) and a power amplifier (RMX 4050HD, QSC Audio). The excitation level for EMA was 15 V_{rms}, which was identified from the harmonic analysis as being in the linear vibrational response regime and ensures adequate signal to noise ratio to characterize the modal peaks.

The vibration response was measured from a grid of points on the surface of the device using a 3D laser Doppler vibrometer (Polytec, CLV-3D) and acquired by data acquisition software (Data Physics Corp, Signal Calc ACE). Magnitude and phase data from the resulting frequency response functions (FRFs) were imported to modal analysis software (MESCOPE, Vibrant Technology) where they were curve fitted and assigned to the grid points of a wireframe model of the measurement grid, producing animated mode shapes. A complex mode indicator function was applied to the raw signals acquired by the 3D LDV, and the fitted curves were calculated by performing a singular value decomposition of the FRF data. Damping was also estimated from the curve fitted FRFs, with Q estimated from the ratio of the modal frequency and the bandwidth of the modal peak half power points. This data could then be compared with Q values calculated from the IA measurements.

3. Harmonic analysis

Nonlinear vibratory responses are associated with high power ultrasonic transducers operating at high excitation levels and can exhibit as resonance frequency shifts, mechanical losses, amplitude jumps, and excitation of non-tuned modal responses. It is widely accepted that these nonlinearities can be attributed to a combination of structural configurations and the strain dependent properties of the piezoceramic material. However, there has not been previous reports of whether Ti-6Al-4V microstructure affects the nonlinear response of resonant ultrasonic devices.

Each device was driven through a frequency range through resonance at increasing excitation levels. At frequency increments of 5 Hz, a burst sinewave was generated by a function generator (Agilent, 33220 A) and a power amplifier (HFVA-62). The longitudinal response was captured using a 1D laser Doppler vibrometer (Polytec, CFV-055), measuring the normal-to-surface response of the cutting tip. The experiments and data collection were controlled by LABVIEW software (National Instruments).

B. Results and discussion

Generally, for a Langevin transducer, efficiency is achieved by locating the piezoceramic rings at the nodal plane of the tuned mode.[29] The needle configuration in this study is tuned to mode L-T2, so one of the nodal planes is at the central cross section of the piezo stack. The tapering profile of this needle device results in the nodal plane of its L-T1 mode being much closer to the piezo stack than for a simple bar shaped Langevin transducer. Since this provided an opportunity to study responses in two energetically excited modes, the responses in both L-T1 and L-T2 were investigated. Only the L1 mode was considered for the bone cutting device with folded front mass.

1. Impedance analysis

Figure 5 presents the impedance measurements, from which the electromechanical characteristics are derived and listed in Table II. The results show that the resonance frequencies of the devices incorporating DMLS Ti-6Al-4V are consistently higher, which is discussed in Sec. III. In their fundamental mode (L-T1 for the needle device and L1 for the folded front mass device) the devices exhibit very similar, and typical, responses of low coupling coefficient, k_{eff}, and high Q, whereas the tuned L-T2 mode of the needle exhibits much higher k_{eff} and lower Q. Also, k_{eff} is very consistent across all the measurement comparisons between the printed and CNC machined versions of the devices, however, Q is consistently lower, by around 40% for the needle in L-T2 and 60% for the twice folded bone cutting device. This would lend evidence to the concern discussed in Sec. II B, that the microtextures and columnar grain structure of DMLS Ti-6Al-4V, shown in Fig. 1, result in increased losses in the material.

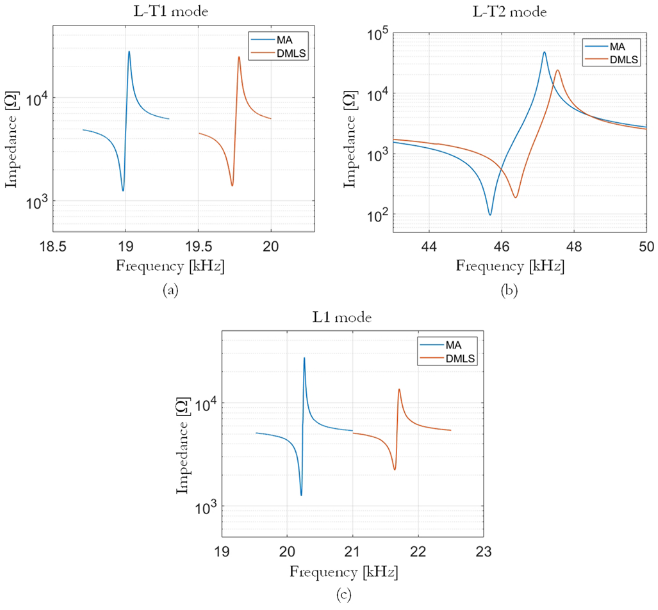

FIG. 5. (Color online) Impedance measurements of (a) L-T1 and (b) L-T2 modes of the needles and (c) L1 mode of the planar twice folded devices, with frequency values reported in Table II.

TABLE II. Parameters extracted from IA of the ultrasonic devices.

	Ultrasonic needles				Planar twice folded devices	
	L-T1 mode		L-T2 mode		L1 mode	
	MA	DMLS	MA	DMLS	MA	DMLS
f_r [Hz]	18 984	19 733	45 680	46 376	20 214	21 643
f_a [Hz]	19 025	19 779	47 180	47 531	20 261	21 706
$\lvert Z_{\mathrm{min}}\rvert$ [Ω]	1237	1384	96	187	1253	2229
k_{eff}	0.07	0.07	0.25	0.22	0.07	0.08
Q_{IA}	791	639	346	211	620	256

Table II also illustrates the trade-off between electromechanical coupling coefficient and quality factor in the CNC machined devices. For resonance tuned ultrasonic devices, high Q is a key requirement, so the reductions in Q are a concern for achieving comparable vibration performance. These reductions in Q can be related to the microstructure, but there is no corresponding increase in k_{eff} in the devices that incorporate DMLS Ti-6Al-4V.

2. Experimental modal analysis

The mode shapes and longitudinal waveforms of the L-T1 and L-T2 modes of the ultrasonic needles and the L1 mode of the planar twice folded bone cutting devices are presented in Fig. 6. The comparison of FEA and EMA results illustrate that the FEA models predict the mode shapes accurately, including their longitudinal amplitude gain profiles, which show the effectiveness of the devices in maximizing displacement at the cutting tip. The amplitude gain is calculated as the ratio of the normalized axial displacement from one end of the device to the other (i.e., surgical tip to back mass).

Measured resonance frequency, amplitude gain, mechanical Q, and nodal plane location are extracted from the EMA data and presented in Table III. For both nodal plane location and amplitude gain, the DMLS printed and CNC machined MA Ti-6Al-4V devices do not exhibit marked differences. When the needle devices are excited in L-T2, the center of the piezoceramic rings is located at a nodal plane, whereas in L-T1 the piezoceramic rings are located 16 mm axially from the nodal plane, resulting in the

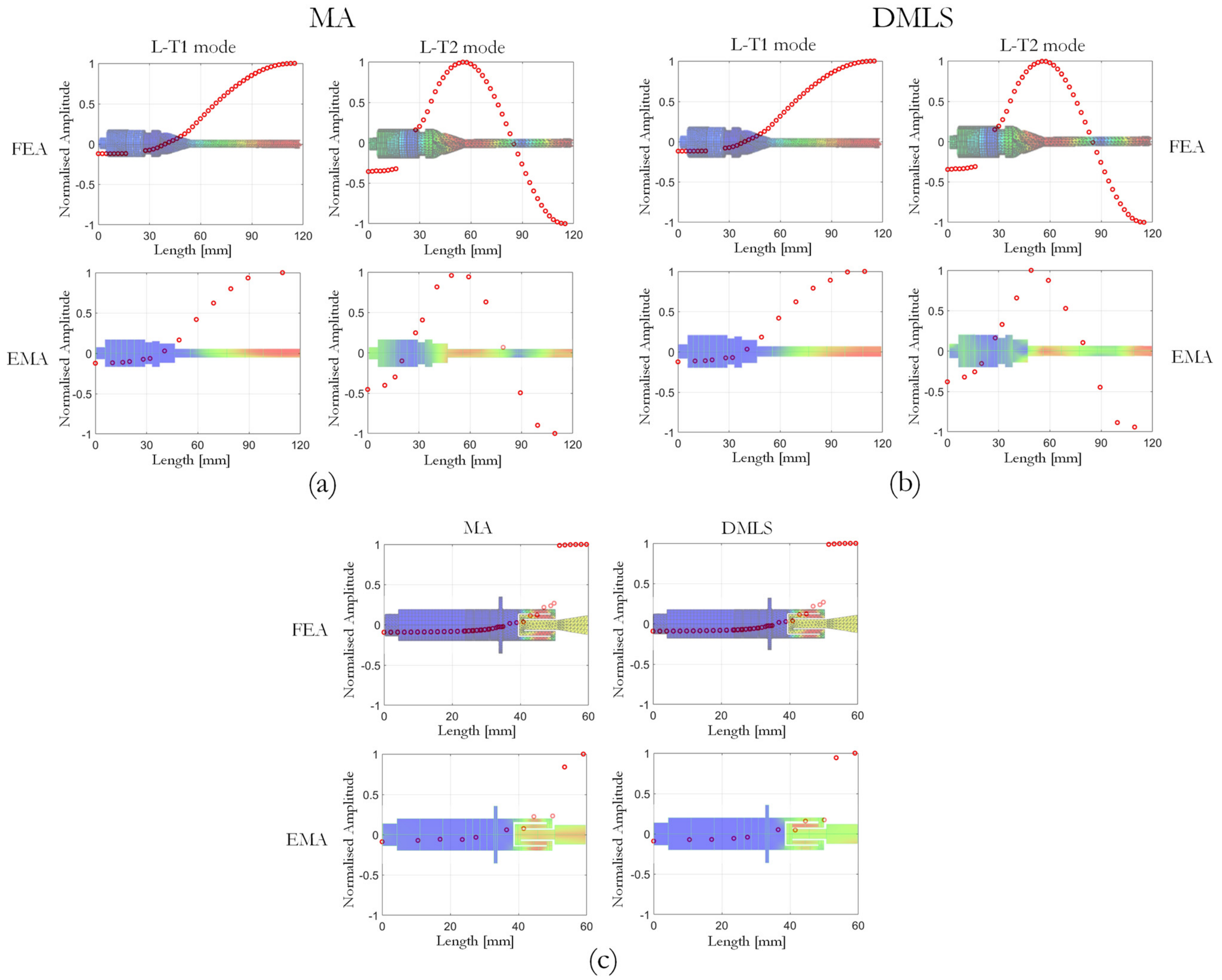

FIG. 6. (Color online) FEA predictions and EMA results of (a) L-T1 (b) L-T2 modes of the ultrasonic needles and (c) L1 mode of the planar twice folded devices. Contour plots of blue to red represent nodal to maximum displacement of the devices, which have the normalized longitudinal gain profile of the associated mode superimposed (red dots).

low k_{eff} values[30] reported in Table II. These differences in nodal location do not exhibit as differences in modal response between MA and DMLS devices. The results show the limitation in the achievable gain from tuning the device in L-T2 mode compared with L-T1 mode, even though the piezoceramic rings are located remote from the nodal plane in L-T1 mode. They also illustrate that the planar twice folded configuration is capable of achieving a high gain in a small device. Importantly, for the high gain modes, L-T1 and L1, gain is affected less than 2%, which could be due to slight differences in the ceramic or assembly and may not be due to the microstructure of the metal.

The curve-fitted frequency response functions (FRFs) of the ultrasonic devices in the 10–60 kHz range are shown in Fig. 7. Estimations of Q from the EMA data, calculated from the FRFs as the ratio of the modal frequency to the

TABLE III. Parameters extracted from EMA of the ultrasonic devices.

	Ultrasonic needles				Cutting blade devices	
	L-T1		L-T2		L1	
	MA (FEA)	DMLS (FEA)	MA (FEA)	DMLS (FEA)	MA (FEA)	DMLS (FEA)
f_r [Hz]	18 975 (18 972)	19 729 (18 918)	45 622 (44 580)	46 358 (44 662)	19 857 (21 485)	21 656 (21 701)
Amplitude gain	8.25	8.22	2.21	2.48	11.41	11.09
Q_{EMA}	1020	1034	300	250	307	495
Center of PZT to node [mm]	16.02	15.97	0.45	2.06	2.43	3.32

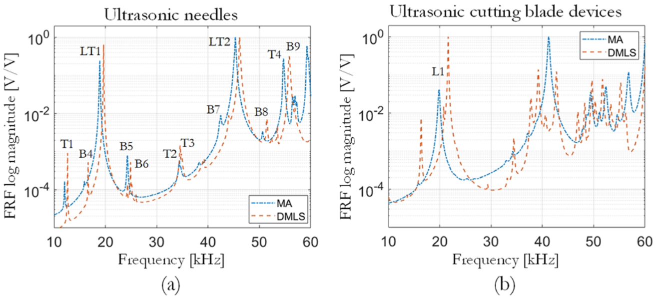

FIG. 7. (Color online) Curve fitted FRFs of MA and DMLS (a) needle devices and (b) planar twice folded cutting devices. Additional mode nomenclature of T (torsional) and B (bending) is used for the needle characterization.

bandwidth of the modal response peak's half-power points, are significantly different from those calculated from the impedance measurements shown in Table II. Furthermore, there are no consistent trends in comparing the values of Q other than the L-T1 mode of the needle device exhibiting the highest Q. The results highlight that Q is affected by the excitation signal and excitation level, which are different in impedance analysis and experimental modal analysis, and neither method is representative of the excitation level of a power ultrasonic device.[31] Having been shown to be poor indicators of losses, neither measurement of Q is a useful indicator of the influence of the metal microstructure on device losses under operating conditions.

For the ultrasonic needles excited in L-T1 and L-T2 modes, and the planar twice folded bone cutting device in L1 mode, the DMLS printed devices consistently have higher resonance frequency than the CNC machined MA devices. Even though their dimensions are the same, the higher longitudinal velocity and lower density of DMLS Ti-6Al-4V, reported in Table I, results in higher resonance frequencies.

For the ultrasonic needles, the FRFs are highly similar, apart from the shift upwards in frequency of all the modes of the DMLS printed needle device in the frequency range of the measurements. All the modes are straightforward to classify and all characterized modes are observed in the response of both devices and are exhibited in the same frequency order. The devices also exhibit comparable frequency separation of the tuned mode, L-T2, from the neighboring bending modes, B7 and B8.

Conversely, there are significant differences in the responses of the two cutting devices incorporating a planar twice folded front mass. The CNC machined device has clear modal peaks with a number of smaller peaks just visible in the response. In the response of the device with DMLS Ti-6Al-4V, all these peaks become more dominant. This is typical of the vibrational response of a structure with multiple beam-like substructures,[32] where a response with a small number of dominant response peaks indicates a highly symmetrical structure and the response exhibiting many response peaks indicates a structure with significant asymmetry. In this bone cutting device, the folds of the front mass are the beam-like substructures, which will exhibit multiple modes (in a mode family), each with a frequency response dominated by a different substructural element. The FRF indicates that the CNC machined device has a high level of symmetry and one modal response dominates for each mode family, whereas the printed Ti-6Al-4V device has significant levels of asymmetry and more than one mode in each mode family is responsive.

To confirm this, the planar twice folded front masses were examined in the MSA-100–3D micro-system analyzer (Polytec, Germany) with ×10 magnification. The poorer surface quality and the asymmetries in the geometry can be clearly seen in the image of the DMLS Ti-6Al-4V front mass in Fig. 8, where particularly the outer folds exhibit some curvature and width variations. For the CNC machined device, the wall thicknesses and gaps are much more consistent. A further concern with asymmetries in this type of structure, and the associated frequency mismatch in the vibrational response of the substructural elements, is the potential for stress concentrations. The modal responses of members of a family of modes each exhibits higher vibrational displacement in a different element of the substructure (or fold of the front mass in this case) leading to asymmetrical oscillatory stress amplitudes in the front mass. These are exacerbated in resonance tuned ultrasonic devices due to the high excitation levels and vibrational displacements. After exciting the device for the impedance analysis and experimental modal analysis measurements, where excitation levels are low, no cracks in the front mass were observed. Importantly, the results highlight how the vibrational modal response of one DMLS device is significantly affected by the manufacturing method itself, whereas the other is not.

3. Harmonic analysis

The longitudinal vibrational response is shown in Fig. 9 at excitation levels incremented from 3 to 120 $\mathrm{V_{pp}}$ (needle devices) and 140 $\mathrm{V_{pp}}$ (cutting devices). The first observations are that the needle L-T1 mode and cutting device L1 mode exhibit highly linear longitudinal displacement responses, with less than 0.05% change in frequency in the range of excitation levels measured, whereas the L-T2 mode of the needle exhibits a softening nonlinear response even at the low displacement amplitudes excited. Linearity is exhibited as a constant resonance frequency and symmetry in the displacement-frequency response about the resonance frequency, whereas a softening nonlinear response exhibits as a

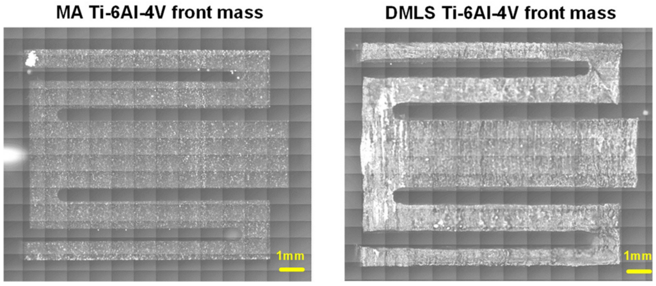
MA Ti-6Al-4V front mass

DMLS Ti-6Al-4V front mass

FIG. 8. (Color online) Image of the planar twice folded features of the CNC MA and DMLS front masses with ×10 magnification.

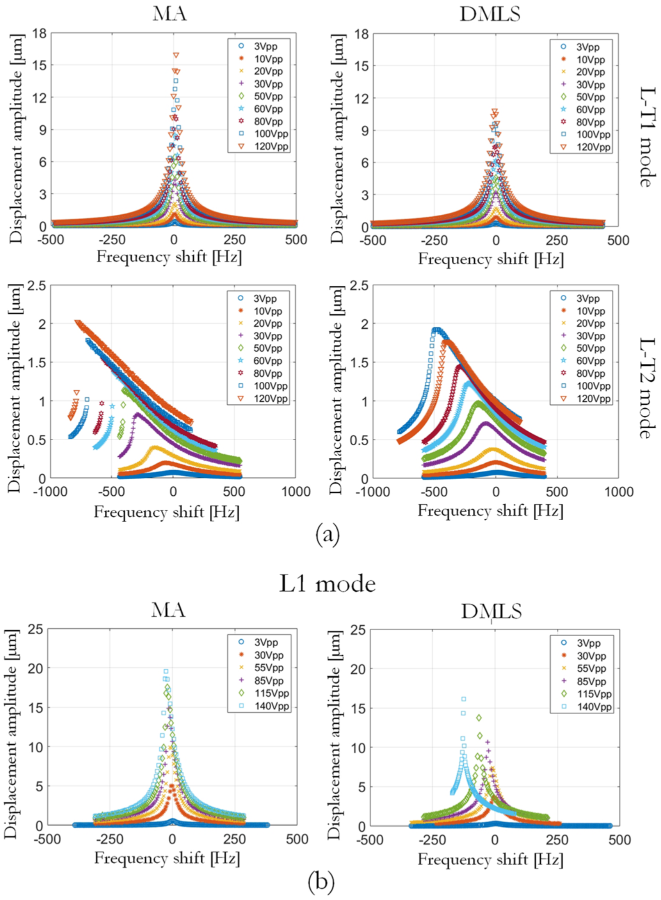

(a)

(b)

FIG. 9. (Color online) Longitudinal displacement response of the MA and DMLS Ti-6Al-4V (a) needle devices and (b) cutting devices.

decrease in resonance frequency with excitation level with a left-bending backbone curve of the displacement-frequency response. Additionally, the L1 response of the DMLS Ti-6Al-4V cutting device shows a linear (symmetric) response at each excitation level but for each measurement the resonance frequency has decreased.

The linear displacement response of the needle L-T1 mode is a result of the piezoceramic rings being located away from the nodal plane (16 mm in Table III), and the effect of this location on linearity is consistent for the MA and DMLS devices. This means the stress in the piezoceramic rings is reduced compared to a device operating with the piezoceramic located at the nodal plane. The piezoceramic is therefore likely not operating in the stress regime where nonlinearity of the piezoelectric properties is exhibited in the response. Although the coupling efficiency of the piezoelectric material is considerably reduced in this configuration, it is observed that the displacement achieved in the L-T1 mode is 6 to 8 times that achieved in the L-T2 mode at the highest excitation level in the harmonic analysis measurements.

The needle in its tuned L-T2 mode, where the piezoceramic rings are located at the nodal plane, exhibits the nonlinear response typical of slender resonance ultrasonic devices driven at high excitation levels. The response is affected by a combination of the excitation level dependence of the piezoelectric properties and the shape of the front mass.[33] The MA device exhibits a resonance frequency decrease in 765 Hz as compared to 480 Hz for the DMLS device at the highest excitation level, but a similar vibrational displacement amplitude of 2 μm is achieved. It is expected that the columnar grains, microtextures, and increased porosity of DMLS could be assisting in reducing the severity of the nonlinearity. A weaker nonlinearity provides some benefit in terms of the ease of frequency tracking of a device in operation.

For the linear responses, the CNC machined MA devices achieve a higher vibrational displacement than the DMLS devices, 16 μm compared with 10.5 μm for the needle at 120 $\mathrm{V_{pp}}$, and 20 μm compared with 16 μm at 140 $\mathrm{V_{pp}}$ for the cutting device. This is explained by the microstructure of MA, with globular grains and a small grain size range being associated with lower material damping than the columnar grains and microtextures of the DMLS. However, the response of the DMLS cutting device with twice folded front mass is consistent with the initiation of a crack that is growing as the excitation level is increased. Although the response associated with each frequency sweep through resonance is highly symmetric at each excitation level, the decrease in stiffness as the crack grows under cyclic oscillations at each higher excitation level results in a concomitant reduction in the resonance frequency.

C. Post harmonic analysis inspection of planar twice folded front mass

A further investigation of the DMLS Ti-6Al-4V cutting device was initiated to confirm the implication of the harmonic analysis, that the device had developed one or multiple cracks. First, the impedance was re-measured and the results of the impedance measurements, before and after all the harmonic analysis experiments were completed, are shown in Fig. 10. It is observed that the impedance magnitude has increased significantly at the resonance frequency and the resonance frequency has decreased by more than 1.5 kHz, both being consistent with the presence of a crack.

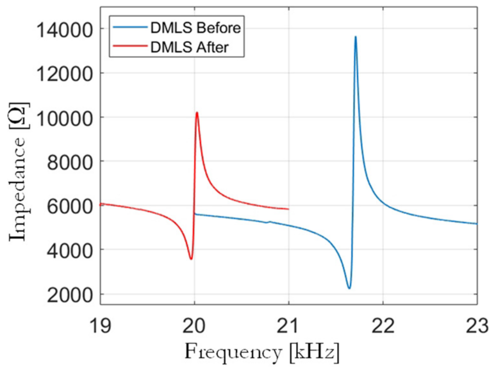

FIG. 10. (Color online) Impedance of the DMLS Ti-6Al-4V cutting device measured before and after high excitation level harmonic analysis experiments.

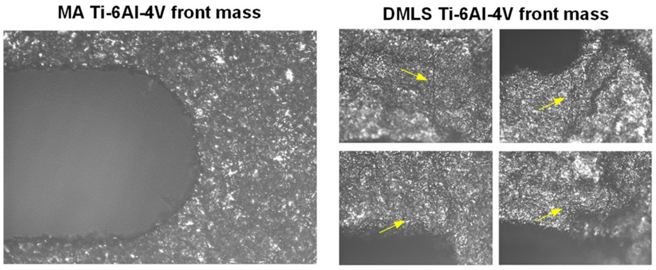

FIG. 11. (Color online) Microscope inspection with ×10 magnification of CNC machined MA and DMLS Ti-6Al-4V planar twice folded front masses with yellow arrows indicating the presence of cracks.

An inspection (Fig. 11) of the DMLS Ti-6Al-4V planar twice folded front mass clearly shows that multiple cracks have been initiated around the curved surface of the gaps between folds. The CNC machined MA front mass, on the other hand, is devoid of cracks.

Cracks are likely to be initiated at defect sites around the weaker and more poorly bonded columnar grains of the Ti-6Al-4V material[34] and as a result of poor surface finish. Also, it is known that porosity arises in layer-based additive printing manufacturing processes which results in deterioration of the material properties.[35] From macroscopic experiments and microstructure analysis, it has been revealed that pores can become nucleation sites for adiabatic shear bands and microcracks.[35,36] If these pores are perpendicular to the loading direction, high stress concentrations will result, from which fatigue cracks can propagate.[37] Another contributing factor of poor fatigue performance under high excitation levels and high frequency cycling of the DMLS material, is the as-built surface roughness which behaves like multiple short cracks and stress concentrators.[38] For DMLS Ti-6Al-4V, the as-built parts without surface machining exhibit fatigue performance of 40%–50% of that achieved after machining.[39,40] Furthermore, the presence of residual stresses, as a result of laser-based additive manufacturing processes with high thermal gradients, is also a cause of crack initiation.[41] Tensile residual stresses are largely distributed on the surface or subsurface of the as-built part,[42] which significantly contributes to poor fatigue performance compared to compressive residual stresses.[43]

To improve the surface quality and increase the fatigue strength of additive manufactured Ti-6Al-4V material,[44–46] machining post-processes can be used, such as centrifugal finishing, shot peening, laser polishing, linishing, and chemical etching.[47] However, one aim of this study was to verify if 3D printing could potentially be adopted for devices with internal features, such as slots, voids, and lumens, where it would be much more challenging to use secondary subtractive processing techniques, unless they were fully integrated with the 3D printing process itself.

V. CONCLUSION

Results have been presented to compare how the use of CNC machined mill annealed Ti-6Al-4V and DMLS Ti-6Al-4V for the end masses affect the impedance and vibrational response of two different prototype ultrasonic surgical devices, an ultrasonic needle operating in a longitudinal-torsional mode and an ultrasonic surgical cutting device with a twice folded front mass configuration. The aim was to investigate the feasibility of adopting DMLS Ti-6Al-4V for the metal end masses to enable innovations in ultrasonic surgical devices that incorporate more complex geometries, especially for miniaturization.

Through characterization of the devices using impedance analysis, experimental modal analysis, and harmonic analysis, it was demonstrated that ultrasonic needle devices that incorporated CNC machined MA and DMLS Ti-6Al-4V exhibited very similar vibrational responses in both EMA and harmonic analysis measurements. The material microstructure of the DMLS resulted in a slightly higher resonance frequency and lower displacement amplitude at the needle tip. Where a nonlinear response was exhibited in the L-T2 mode, the microstructure resulted in a weaker nonlinearity. Overall, the potential of 3D printed metal masses to replace CNC machined metal masses was confirmed for this ultrasonic device.

For the cutting device with twice-folded front mass, the dependance of the response on a high level of symmetry, to avoid excitation of mode families, resulted in high modal density in the frequency response function of the DMLS device. The incorporation of a twice-folded front mass is shown to deliver a linear vibrational response at the high excitation levels associated with power ultrasonic devices. However, in the case of the DMLS device the response was indicative of one or more cracks initiating and growing as the excitation level increased and this was verified by inspection.

DMLS Ti-6Al-4V has been shown to be a viable alternative for the end masses of power ultrasonic surgical devices that have complex shapes and features, but not where those features are substructures requiring a high degree of symmetry. Ideally, to enable adoption of DMLS Ti-6Al-4V in power ultrasonic surgical devices that incorporate features such as folds and slots, improvements in the build quality, control of porosity, and surface finish are necessary. Although there are multiple post-processing methods available that can improve surface finish and fatigue strength, these become very challenging to incorporate where the device features are highly complex or internal to the device parts. Further research is required to investigate the relative performance of devices incorporating DMLS Ti-6Al-4V under the loading conditions typical of surgical operations.

ACKNOWLEDGMENTS

This work was supported by an EPSRC Programme Grant (Ultrasurge–Surgery enabled by Ultrasonics, EP/R045291/1).

[1] G. Pavlíková, R. Foltán, M. Horká, T. Hanzelka, H. Borunská, and J. Šedý, "Piezosurgery in oral and maxillofacial surgery," Int. J. Oral Maxillofac. Surg. 40(5), 451–457 (2011).

[2] T. Vercellotti and A. Podesta, "Orthodontic microsurgery: A new surgically guided technique for dental movement," Int. J. Periodontics Restorative Dent. **27**, 325–331 (2007).

[3] E. S. Flamm, J. Ransohoff, D. Wuchinich, and A. Broadwin, "Preliminary experience with ultrasonic aspiration in neurosurgery," Neurosurgery **2**, 240–245 (1978).

[4] R. Al-Mahfoudh, E. Qattan, J. R. Ellenbogen, M. Wilby, C. Barrett, and T. Pigott, "Applications of the ultrasonic bone cutter in spinal surgery-our preliminary experience," Br. J. Neurosurg. **28**, 56–60 (2014).

[5] F. M. Duerr, H. B. Seim, A. L. Bascunãń, R. H. Palmer, and J. Easley, "Piezoelectric surgery—A novel technique for laminectomy," J. Investig. Surg. **28**, 103–108 (2015).

[6] M. Y. Noordin, N. Jiawkok, P. Y. M. W. Ndaruhadi, and D. Kurniawan, "Machining of bone: Analysis of cutting force and surface roughness by turning process," Proc. Inst. Mech. Eng. Part H. J. Eng. Med. **229**, 761–768 (2015).

[7] A. R. Moritz and F. C. Henriques, "Studies of thermal injury: II. The relative importance of time and surface temperature in the causation of cutaneous burns," Am. J. Pathol. **23**, 695–720 (1947).

[8] K. Alam, M. Khan, and V. V. Silberschmidt, "Analysis of forces in conventional and ultrasonically assisted plane cutting of cortical bone," Proc. Inst. Mech. Eng. Part H. J. Eng. Med. **227**, 636–642 (2013).

[9] G. Eggers, J. Klein, J. Blank, and S. Hassfeld, "Piezosurgery®: An ultrasound device for cutting bone and its use and limitations in maxillofacial surgery," Br. J. Oral Maxillofac. Surg. **42**(5), 451–453 (2004).

[10] D. J. Ewins, *Modal Testing: Theory, Practice and Application* (Wiley, New York, 2000).

[11] A. Mathieson, A. Cardoni, N. Cerisola, and M. Lucas, "Understanding nonlinear vibration behaviours in high-power ultrasonic surgical devices," Proc. R. Soc. A Math. Phys. Eng. Sci. **471**, 20140906 (2015).

[12] A. Zolfagharian, A. Z. Kouzani, S. Y. Khoo, A. A. A. Moghadam, I. Gibson, and A. Kaynak, "Evolution of 3D printed soft actuators," Sens. Act. A Phys. **250**, 258–272 (2016).

[13] M. R. Haberman, "Acoustic metamaterials and additive manufacturing," J. Acoust. Soc. Am. **145**, 1812 (2019).

[14] Z. Chen, X. Song, L. Lei, X. Chen, C. Fei, C. T. Chiu, X. Qian, T. Ma, Y. Yang, K. Shung, and Y. Chen, "3D printing of piezoelectric element for energy focusing and ultrasonic sensing," Nano Energy **27**, 78–86 (2016).

[15] B. Zhu, J. M. F. Guerreiro, Y. Zhang, B. P. Tiller, and J. F. C. Windmill, "Additive manufacturing (AM) capacitive acoustic and ultrasonic transducers using a commercial direct light processing (DLP) printer," IEEE Sens. J. **20**, 1770–1777 (2020).

[16] J. Cheng, Y. Chen, J. W. Wu, X. R. Ji, and S. H. Wu, "3D printing of BaTiO3 piezoelectric ceramics for a focused ultrasonic array," Sensors **19**, 4078 (2019).

[17] A. Mathieson, B. Tyson, and A. Bond, "The demonstration of additive manufacture in power ultrasonic and sonar transducers," IEEE Trans. Ultrason. Ferroelectr. Freq. Control **67**, 817–824 (2020).

[18] R. E. Lewis, J. G. Bjeletich, T. M. Morton, and F. A. Crossley, "Effect of cooling rate on fracture behavior of mill-annealed Ti-6Al-4V," Cracks Fract. ASTM STP 601, Am. Soc. Test. Mater. 371–390 (1976).

[19] R. P. Mulay, J. A. Moore, J. N. Florando, N. R. Barton, and M. Kumar, "Microstructure and mechanical properties of Ti-6Al-4V: Mill-annealed versus direct metal laser melted alloys," Mater. Sci. Eng. A **666**, 43–47 (2016).

[20] P. P. Paul, M. Fortman, H. M. Paranjape, P. M. Anderson, A. P. Stebner, and L. C. Brinson, "Influence of structure and microstructure on deformation localization and crack growth in NiTi shape memory alloys," Shape Mem. Superelasticity **4**, 285–293 (2018).

[21] D. A. Wang, W. Y. Chuang, K. Hsu, and H. T. Pham, "Design of a Bézier-profile horn for high displacement amplification," Ultrasonics **51**, 148–156 (2011).

[22] A. Bhattacharjee, A. L. Pilchak, O. I. Lobkis, J. W. Foltz, S. I. Rokhlin, and J. C. Williams, "Correlating ultrasonic attenuation and microtexture in a near-alpha titanium alloy," Met. Mater. Trans. A Phys. Metall. Mater. Sci. **42**, 2358–2372 (2011).

[23] D. Yuan, S. Shao, C. Guo, C. F. Jiang, and J. Wang, "Grain refining of Ti-6Al-4V alloy fabricated by laser and wire additive manufacturing assisted with ultrasonic vibration," Ultrason. Sonochem. **73**, 105472 (2021).

[24] M. Wilkie and M. Lucas, "The effect of Ti-6Al-4V microstructure on the performance of ultrasonic soft tissue cutting tips," Proc. Mtgs. Acoust. **32**, 020010 (2017).

[25] A. A. Razek and B. Y. Huang, "Lesions of the petrous apex: Classification and findings at CT and MR imaging," Radiographics **32**, 151–173 (2012).

[26] R. Cleary and M. Lucas, "Comparison of longitudinal-mode and longitudinal-torsional mode ultrasonic bone biopsy devices," IEEE Int. Ultrason. Symp. IUS 1–9 (2018).

[27] S. Sherrit, M. Badescu, X. Bao, Y. Bar-Cohen, and Z. Chang, "Novel horn designs for power ultrasonics," Proc. IEEE Ultrason. Symp. **3**, 2263–2266 (2004).

[28] T. M. Mower, "Degradation of titanium 6Al–4V fatigue strength due to electrical discharge machining," Int. J. Fatigue **64**, 84–96 (2014).

[29] A. Caronti, R. Carotenuto, and M. Pappalardo, "Electromechanical coupling factor of capacitive micromachined ultrasonic transducers," J. Acoust. Soc. Am. **113**, 279–288 (2003).

[30] V. K. Astashev, K. A. Pichugin, X. Li, A. Meadows, and V. I. Babitsky, "Resonant tuning of Langevin transducers for ultrasonically assisted machining applications," IEEE Trans. Ultrason. Ferroelectr. Freq. Control **67**, 1888–1896 (2020).

[31] D. A. DeAngelis, "Predicting the displacement gain from the mechanical quality factor in ultrasonic transducers," Phys. Procedia **87**, 2–9 (2016).

[32] A. Mathieson, A. Cardoni, N. Cerisola, and M. Lucas, "The influence of piezoceramic stack location on nonlinear behavior of Langevin transducers," IEEE Trans. Ultrason. Ferroelectr. Freq. Control **60**, 1126–1133 (2013).

[33] C. Chesnais, C. Boutin, and S. Hans, "Effects of the local resonance in bending on the longitudinal vibrations of reticulated beams," Wave Motion **57**, 1–22 (2015).

[34] K. F. Walker, Q. Liu, and M. Brandt, "Evaluation of fatigue crack propagation behaviour in Ti-6Al-4V manufactured by selective laser melting," Int. J. Fatigue **104**, 302–308 (2017).

[35] S. Liu and Y. C. Shin, "Additive manufacturing of Ti6Al4V alloy: A review," Mater. Des. **164**, 107552 (2019).

[36] N. Biswas, J. L. Ding, V. K. Balla, D. P. Field, and A. Bandyopadhyay, "Deformation and fracture behavior of laser processed dense and porous Ti6Al4V alloy under static and dynamic loading," Mater. Sci. Eng. A **549**, 213–221 (2012).

[37] P. H. Li, W. G. Guo, W. D. Huang, Y. Su, X. Lin, and K. B. Yuan, "Thermomechanical response of 3D laser-deposited Ti-6Al-4V alloy over a wide range of strain rates and temperatures," Mater. Sci. Eng. A **647**, 34–42 (2015).

[38] E. Wycisk, A. Solbach, S. Siddique, D. Herzog, F. Walther, and C. Emmelmann, "Effects of defects in laser additive manufactured Ti-6Al-4V on fatigue properties," Phys. Procedia **56**, 371–378 (2014).

[39] M. Suraratchai, J. Limido, C. Mabru, and R. Chieragatti, "Modelling the influence of machined surface roughness on the fatigue life of aluminium alloy," Int. J. Fatigue **30**, 2119–2126 (2008).

[40] T. M. Mower and M. J. Long, "Mechanical behavior of additive manufactured, powder-bed laser-fused materials," Mater. Sci. Eng. A **651**, 198–213 (2016).

[41] D. Greitemeier, C. Dalle Donne, F. Syassen, J. Eufinger, and T. Melz, "Effect of surface roughness on fatigue performance of additive manufactured Ti–6Al–4V," Mater. Sci. Technol. (United Kingdom) **32**, 629–634 (2016).

[42] P. Edwards and M. Ramulu, "Fatigue performance evaluation of selective laser melted Ti-6Al-4V," Mater. Sci. Eng. A **598**, 327–337 (2014).

[43] P. J. Golden, R. John, and W. J. Porter, "Investigation of variability in fatigue crack nucleation and propagation in alpha + beta Ti-6Al-4V," Procedia Eng. **2**, 1839–1847 (2010).

[44] M. Kahlin, H. Ansell, and J. J. Moverare, "Fatigue behaviour of notched additive manufactured Ti6Al4V with as-built surfaces," Int. J. Fatigue **101**, 51–60 (2017).

[45] D. Greitemeier, F. Palm, F. Syassen, and T. Melz, "Fatigue performance of additive manufactured TiAl6V4 using electron and laser beam melting," Int. J. Fatigue **94**, 211–217 (2017).

[46] J. Günther, D. Krewerth, T. Lippmann, S. Leuders, T. Troster, A. Weidner, H. Biermann, and T. Niendort, "Fatigue life of additively manufactured Ti-6Al-4V in the very high cycle fatigue regime," Int. J. Fatigue **94**, 236–245 (2017).

[47] M. Kahlin, H. Ansell, D. Basu, A. Kerwin, L. Newton, B. Smith, and J. J. Moverare, "Improved fatigue strength of additively manufactured Ti6Al4V by surface post processing," Int. J. Fatigue **134**, 105497 (2020).